Frustration-driven Na^+ migration in Na_3OBH_4

Qinfu Zhao(赵钦福), Min Jiang(蒋敏), Junrui Tong(同俊瑞), Weiguo Wang(王伟国), Shuyao Cao(曹舒尧), Ping Zhang(张萍), Zhihui He(何智慧), Fang Kang(康芳), Qi Song(宋齐)

Citation: Chin. Phys. B. 35, 108202 (2026). DOI: 10.1088/1674-1056/ae4c6a | CSTR: 32038.14.CPB.ae4c6a
http://cpb.iphy.ac.cn; http://iopscience.iop.org/cpb

What follows is a list of articles you may be interested in

Defect chemistry engineering of Ga-doped garnet electrolyte with high stability for solid-state lithium metal batteries

Sihan Chen(陈思汗), Jun Li(黎俊), Keke Liu(刘可可), Xiaochen Sun(孙笑晨), Jingwei Wan(万京伟), Huiyu Zhai(翟慧宇), Xinfeng Tang(唐新峰), Gangjian Tan(谭刚健)
Chin. Phys. B. 33, 088203 (2024). DOI: 10.1088/1674-1056/ad41b9

Interface and mechanical degradation mechanisms of the silicon anode in sulfide-based solid-state batteries at high temperatures

Qiuchen Wang(王秋辰), Yuli Huang(黄昱力), Jing Xu(许晶), Xiqian Yu(禹习谦), Hong Li(李泓), Liquan Chen(陈立泉)
Chin. Phys. B. 33, 088201 (2024). DOI: 10.1088/1674-1056/ad5276

A novel order-reduced thermal-coupling electrochemical model for lithium-ion batteries

Yizhan Xie(谢奕展), Shuhui Wang(王舒慧), Zhenpo Wang(王震坡), Ximing Cheng(程夕明)
Chin. Phys. B. 33, 058203 (2024). DOI: 10.1088/1674-1056/ad1f52

Structural, electronic, and Li-ion mobility properties of garnet-type $Li_7La_3Zr_2O_{12}$ surface: An insight from first-principles calculations

Jing-Xuan Wang(王靖轩), Bao-Zhen Sun(孙宝珍), Mei Li(李梅), Mu-Sheng Wu(吴木生), Bo Xu(徐波)
Chin. Phys. B. 32, 068201 (2023). DOI: 10.1088/1674-1056/acc05d

Liquid-phase synthesis of Li_2S and Li_3PS_4 with lithium-based organic solutions

Jieru Xu(许洁茹), Qiuchen Wang(王秋辰), Wenlin Yan(闫汶琳), Liquan Chen(陈立泉), Hong Li(李泓), Fan Wu(吴凡)
Chin. Phys. B. 31, 098203 (2022). DOI: 10.1088/1674-1056/ac7459

Frustration-driven Na^+ migration in Na_3OBH_4

Qinfu Zhao(赵钦福)[1,2], Min Jiang(蒋敏)[1], Junrui Tong(同俊瑞)[1], Weiguo Wang(王伟国)[1], Shuyao Cao(曹舒尧)[1], Ping Zhang(张萍)[1], Zhihui He(何智慧)[1,2], Fang Kang(康芳)[1,2,†], and Qi Song(宋齐)[3]

[1] *College of Physics and Electronic Information, Yan'an University, Yan'an* 716000, *China*
[2] *Key Laboratory of Advanced Optoelectronic Materials and Devices of Higher Education Institutions in Shaanxi, Yan'an University, Yan'an* 716000, *China*
[3] *Shaanxi Key Laboratory for Theoretical Physic Frontiers, Institute of Modern Physics, Northwest University, Xi'an* 710069, *China*

(Received 18 December 2025; revised manuscript received 6 February 2026; accepted manuscript online 3 March 2026)

Strategies to improve ionic conductivity in solid electrolytes focus predominantly on the static interactions between polyanions and cations, while the dynamic behavior of polyanions has been largely overlooked. In this work, we employ machine-learning molecular dynamics (MLMD) to explore the coupling between Na^+ migration and $[BH_4]^-$ reorientation in Na_3OBH_4. The results show that polyanion reorientations occur at rates about four orders of magnitude higher than Na^+ migrations and exhibit only weak temporal correlation with them, indicating that Na^+ transport does not follow a paddle-wheel mechanism. Analysis of the atomistic energy landscape reveals that $[BH_4]^-$ reorientation induces localized potential fluctuations that split the Na^+ energy states, raising the initial-state energy while lowering the transition-state energy and thereby generating low-barrier migration pathways. Frequency analyses further identify an optimal relation between the fluctuation frequency and Na^+ vibrational modes that enhances low-temperature ionic diffusivity. These results confirm dynamic frustration as a central factor in polyanion-assisted cation transport, providing design guidelines for complex hydride electrolytes.

Keywords: solid electrolytes, machine learning molecular dynamics, dynamic frustration, ion transport, Na_3OBH_4

PACS: 82.45.Gj, 31.15.xv, 31.15.at

DOI: 10.1088/1674-1056/ae4c6a **CSTR:** 32038.14.CPB.ae4c6a

1. Introduction

All-solid-state sodium-ion batteries (ASSSBs) are regarded as promising alternatives for next-generation energy storage technologies, owing to the natural abundance of sodium, its low cost, and inherent safety advantages.[1–5] Sodium superionic conductors (SSICs), which are characterized by rapid carrier migration through rigid crystalline lattices while maintaining structural integrity, are central to the development of high-performance ASSSBs.[6–13] Understanding the physical mechanisms of ion transport in these materials is therefore crucial for designing next-generation SSICs.

Previous studies have suggested that the coupling between carrier migration and polyanion $[AB_y]^{n-}$ reorientation may drive the high ionic conductivity in certain inorganic crystalline materials, which has spurred extensive studies of this mechanism.[14–26] In 2019, Xie *et al.*[18] discovered Na_3OBH_4 with high ionic conductivity of 4.4×10^{-3} S·cm^{-1} and excellent electrochemical performance at room temperature. They proposed that the $[BH_4]^-$ reorientation couples with Na^+ migration through the paddle-wheel effect, leading to enhanced Na^+ migration. However, contrary results were obtained by Famprikis *et al.*,[27] whose impedance spectroscopy and *ab initio* molecular dynamics (AIMD) simulations indicated markedly reduced conductivity in Na_3OBH_4. Limited by computational costs, their study employed short-timescale molecular dynamics (MD) simulations at high temperatures (> 700 K), estimating room-temperature Na^+ migration via Arrhenius equation extrapolation. This strategy requires that carrier migration strictly obey the Arrhenius equation and that high-temperature conductivity measurements maintain sufficient precision. Otherwise, significant errors will arise in the ion diffusion coefficients at low temperatures.[28]

This work aims to clarify these debates by using machine-learning molecular dynamics (MLMD) simulations to systematically investigate relatively low-temperature Na^+ migration behavior in Na_3OBH_4. Although AIMD achieves density functional theory (DFT)-level accuracy and can provide atomic-scale insights into the thermally activated processes in Na_3OBH_4, its high computational cost severely restricts system sizes and simulation time.[28,29] Classical force-field approaches enable extended spatiotemporal sampling but often lack reliability in complex inorganic systems.[30] The MLMD method bridges the accuracy-efficiency gap by using machine-learning interatomic potentials (MLPs) trained on first-principles data.[31–35] This method achieves near-DFT precision while extending simulations to larger system sizes and longer timescales and enables a quantitative description of the true detailed coupling between Na^+ migration and $[BH_4]^-$ reorientation. The MLMD simulation results quantify the

†Corresponding author. E-mail: 825384361@yau.edu.cn

© 2026 Chinese Physical Society and IOP Publishing Ltd. All rights, including for text and data mining, AI training, and similar technologies, are reserved.

Arrhenius behavior of carriers and clarify how Na^+ migration is coupled to $[BH_4]^-$ reorientation in the low-temperature regime.

2. Methods

All the DFT calculations were performed using the projector augmented wave (PAW) method within the Vienna *ab initio* simulation package (VASP).[36,37] The exchange-correlation effects were treated with the generalized gradient approximation (GGA) in the Perdew–Burke–Ernzerhof (PBE) functional.[38] The plane wave cut off energy was set to 700 eV and a *k*-point density of at least 64/Å^{-3} was used. Structural relaxation was performed until atomic forces reached below 10^{-3} eV/Å, and the total energy converged within 10^{-6} eV/atom. AIMD simulations were performed to generate initial configurations for training the MLPs. These simulations used the canonical (NVT) ensemble with Nosé–Hoover thermostats at 700–900 K, a 1 fs time step, and the Γ-point *k*-mesh.[39] A $2 \times 2 \times 2$ supercell of cubic Na_3OBH_4 (space group $P43m$) containing 0, 1, or 2 Na^+ vacancies was adopted.

The MLPs were constructed using the deep potential generator (DP-GEN) package.[40] Four DP force fields were trained from the AIMD configurations with different network initializations. Short MD simulations were performed using these DP force fields, and the maximum force deviation among the four predictions was computed for each configuration. Configurations with deviations between 0.09 and 0.25 eV/Å were selected as candidates. Up to 100 candidate configurations were randomly selected through DFT evaluation and added to the training set for retraining of DP models. The iterative process was repeated for 18 cycles and was considered converged when the configuration exploration accuracy exceeded 96%.

Classical molecular dynamic simulations were performed in LAMMPS within the NVT ensemble using a Nosé–Hoover thermostat and a 1 fs time step.[41] A $3 \times 3 \times 3$ supercell (236 atoms) with 8.6% Na^+ vacancy concentration, consistent with experiments, was adopted.[18] MD simulations were performed at 400–600 K to ensure sufficient Na^+ migration events while minimizing contributions from H^- quantum tunneling, as the MLPs were trained without nuclear quantum effects. The initial structures were equilibrated for 20 ps at the targeted temperatures, followed by 2 ns MD simulations to quantify the ionic diffusion coefficient until convergence.

3. Results and discussion

3.1. Validation of the MLP force field

The accuracy of the machine-learning potential (MLP) was validated against DFT calculations and experimental structural data.[42–44] The testing sets comprising 1500 configurations sampled from all supercell types yield root-mean-square errors (RMSEs) of 1.87 meV·atom^{-1} for energies and 0.06 eV·Å^{-1} for forces, demonstrating close agreement with DFT benchmarks (Fig. 1). The MLP-predicted lattice parameters and volume for Na_3OBH_4 are in excellent agreement with experimental values, with relative errors of 0.65% and 1.92%, respectively (Table 1). This confirms that the MLPs accurately capture the material's structural properties. These results indicate that the potential reproduces both energetic and structural properties at near-DFT fidelity, ensuring reliable representation of the atomistic interactions. To further assess the accuracy of the MLP for diffusion dynamics, short-time MD simulations were performed at 700 K using both AIMD and MLMD in a $2 \times 2 \times 2$ supercell containing one Na^+ vacancy (each comprising 10000 steps at 2 fs per step). Linear fitting of the mean squared displacement (MSD) curves yields diffusion coefficients of 2.7×10^{-7} cm^2/s and 2.2×10^{-7} cm^2/s for AIMD and MLMD, respectively, showing closely matching values (Fig. S1). These results confirm the reliability of the MLP in capturing diffusion behavior in this system. The validated MLP thus provides a solid foundation for large-scale simulations of Na^+ migration and for probing the coupling between carrier migration and polyanions $[BH_4]^-$ reorientation.

Table 1. Comparison of the lattice constants and volumes predicted by the machine-learned potential (MLP) with the experimental values.

	a (Å)	*b* (Å)	*c* (Å)	Volume (Å^3)
MLP predicted	4.60	4.60	4.60	97.34
Experiment	4.63	4.63	4.63	99.25

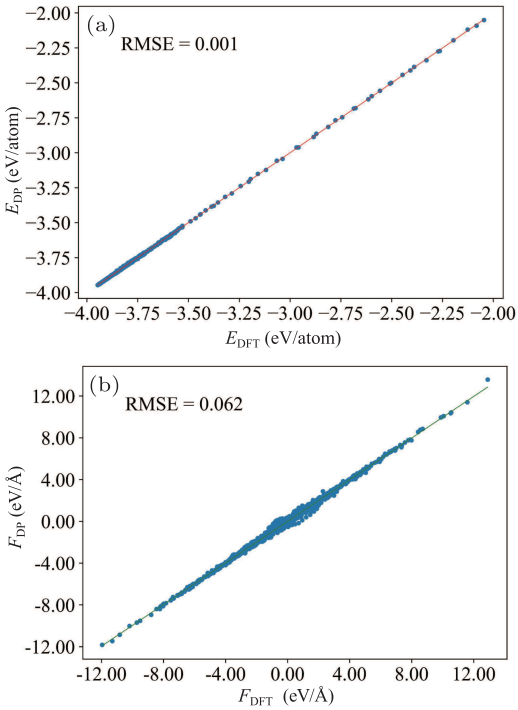

Fig. 1. Comparison of the energies (a) and forces (b) computed by DP models and DFT for the test dataset generated by DP-GEN sampling.

3.2. Ionic diffusion coefficients in Na_3OBH_4

Accurate quantification of Na^+ diffusion in Na_3OBH_4 has been challenging due to the limited timescales ($\sim$ 100 ps) accessible in AIMD, which restricts the number of migration events available for reliable statistical analysis. The construction of MLPs enabled extended MD simulations up to 2 ns, capturing abundant Na^+ migration events at 400–600 K. The MSD profiles exhibit linear behavior (Fig. 2(a)), confirming sufficient sampling and allowing precise calculation of diffusion coefficients for Arrhenius fitting.

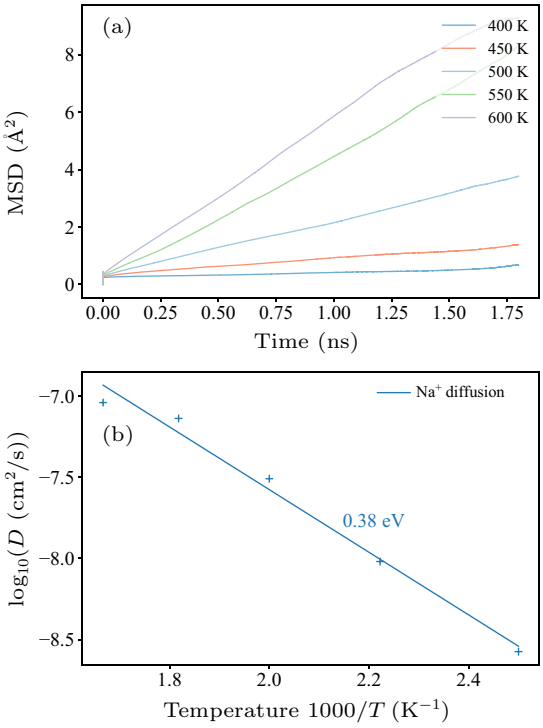

Fig. 2. Na^+ diffusion coefficients obtained from MLMD simulations in Na_3OBH_4. (a) Mean squared displacement (MSD) curves of Na^+ in the temperature range of 400–600 K. (b) Arrhenius plot of the Na^+ diffusion coefficients.

As shown in Fig. 2(b), the Na^+ diffusivity follows an excellent Arrhenius behavior across the simulated temperature range. At 400 K, the Na^+ diffusion coefficient reaches approximately 0.26×10^{-8} cm^2/s, consistent with the AIMD result reported by Famprikis *et al.*[27] The Arrhenius fit yields an apparent activation energy of 0.38 eV, slightly higher than the 0.30 eV obtained from our CI-NEB calculation.[45] This difference arises because the CI-NEB calculation at 0 K does not account for the dynamic scattering of Na^+ by the lattice.

In addition, the calculated activation energy is significantly lower than the experimental value of 0.81 eV from impedance measurements.[27] This can be attributed to factors not fully represented in the simulations: (i) Thermal lattice expansion in experiments enlarges transport pathways, resulting in a steeper Arrhenius slope.[46] This effect is quantified by quasi-harmonic approximation (QHA) calculations performed in our previous work, which reveal a lattice volume expansion from 107 Å^3 (at 300 K) to 116 Å^3 (at 800 K).[45] (ii) The measured activation energy includes the contribution from vacancy formation, as the Na^+ vacancy concentration increases with temperature.[47] This effect is verified by our earlier computational work, which demonstrated the rise of Na^+ vacancy concentration with temperature in Na_3OBH_4 and provided the corresponding vacancy formation energy.[45] (iii) Additional migration barriers from microstructural defects such as grain boundaries and dislocations.[48]

3.3. Correlation between Na^+ migration and $[BH_4]^-$ reorientation

Na^+ migration in Na_3OBH_4 is facilitated by its coupling with the reorientational dynamics of the $[BH_4]^-$ anions. To clarify the degree of such coupling, we first quantified the $[BH_4]^-$ reorientation frequency from the MLMD trajectories. The $[BH_4]^-$ reorientation dynamics are identified through H^- hopping around each B^{3+}, where individual hops correspond to transitions between neighboring regions on the local potential-energy surface.[49] These regions—representing minima separated by narrow transition pathways—were extracted through clustering analysis, enabling direct counting of reorientation events over the simulated temperature range (Fig. 3(a)).[50]

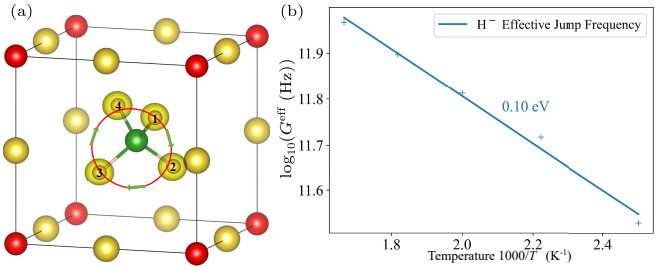

Fig. 3. (a) Schematic illustration of the rotational hopping of H^- around B^{3+} ions. The yellow translucent region represents the high probability density area of H^-. (b) Arrhenius plot of the effective hopping frequency of H^- around B^{3+}. The slope of the linear fit yields the reorientation barrier of $[BH_4]^-$ groups.

The resulting effective hopping frequency of H^- around B^{3+} obeys the Arrhenius relation[49]

$$\Gamma^{\mathrm{eff}} = \nu_0 \, \mathrm{e}^{-\frac{\Delta E}{k_B T}}, \tag{1}$$

where k_B is Boltzmann's constant, T is the temperature in Kelvin, Γ^{eff} is the effective hopping frequency obtained via the counting method described above, ν_0 is the pre-exponential factor — that is, the attempt frequency of H^- hopping around B^{3+} — and its explicit value is not required for this analysis, and the reorientation barrier ΔE is extracted solely from the slope of the Arrhenius plot across the studied temperature range. The resulting barrier is approximately 0.1 eV, substantially lower than the Na^+ migration barrier (Fig. 3(b)). As a result, $[BH_4]^-$ reorientation occurs at rates about four orders of magnitude higher than Na^+ migration, indicating that $[BH_4]^-$ reorientation is too rapid and too weakly synchronized with Na^+ migration to support a paddle-wheel mechanism.

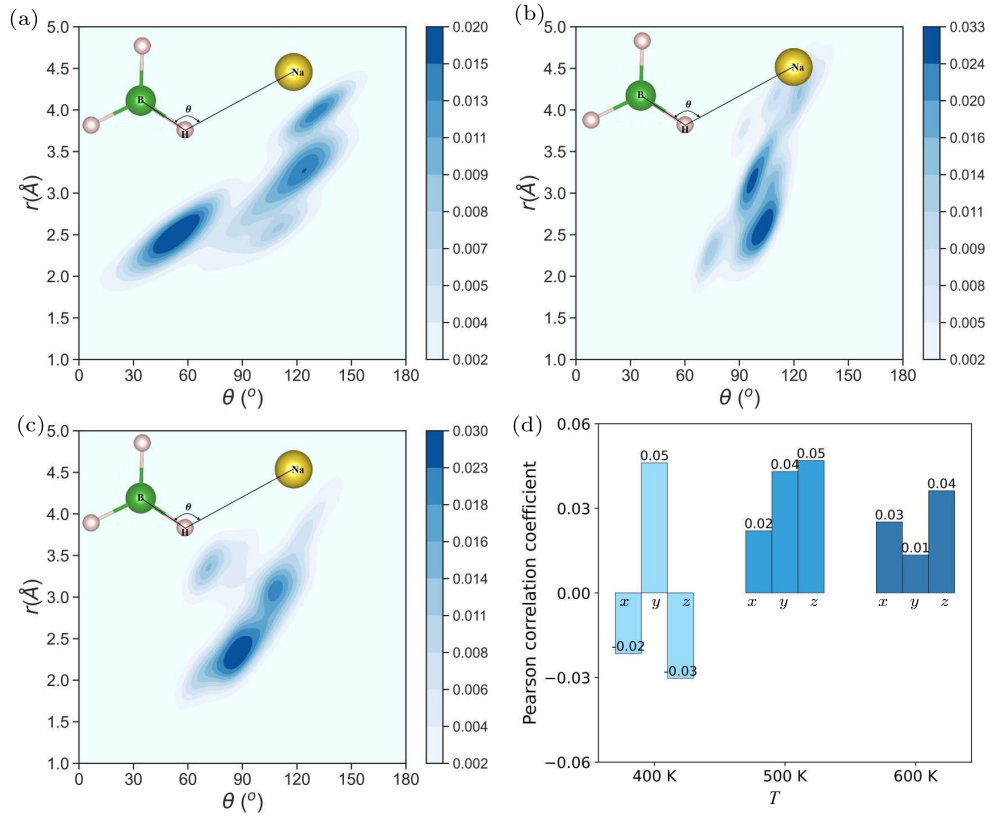

Fig. 4. The relationships between $[BH_4]^-$ anion groups and their adjacent Na^+ during Na^+ migration. 2D probability density distribution ($\rho^{2D}_{r,\theta}$) of BHNa angles θ and distance r between H and Na^+ at (a) 400 K, (b) 500 K, and (c) 600 K, respectively; (d) Pearson correlation coefficients between angular velocity vectors of H in rotational $[BH_4]^-$ anions and their adjacent Na^+.

In addition, the spatiotemporal correlation between Na^+ migration and $[BH_4]^-$ reorientation was analyzed. Figures 4(a)–4(c) present two-dimensional probability density distributions ($\rho^{2D}_{r,\theta}$) of the B–H–Na angle θ and the distance r between H and adjacent Na^+ tracked during representative Na^+ migration events at 400, 500, and 600 K, respectively. The distributions for all rotational $[BH_4]^-$ are highly delocalized and dispersed across most of the (r, θ) space, indicating weak dynamical coupling between the $[BH_4]^-$ anion and adjacent Na^+. In contrast, strong polyanion–cation coupling would result in a probability density localized into a clustered spot. For a quantitative evaluation, Pearson correlation coefficients were calculated for each Cartesian component (x, y, z) between the angular velocity vectors of B–H–Na angle θ (Fig. 4(d)). All correlation coefficients exhibit absolute values below 0.10, demonstrating that Na^+ migration is essentially uncorrelated with $[BH_4]$ anion rotation. This provides direct evidence against the existence of a paddle-wheel mechanism in Na_3OBH_4.

3.4. Na^+ migration facilitated by dynamic frustration

Although Na^+ migration events show no clear spatiotemporal coupling with $[BH_4]^-$ reorientation, the highly reorientable $[BH_4]^-$ groups actively generate intrinsic structural disorder.[51–53] We propose that the reorientation of $[BH_4]^-$ groups disrupts long-range ordering in the crystal and distorts the local energy landscape. Na^+ cations are no longer tightly bound to their equilibrium positions but become increasingly delocalized. Ordered $[BH_4]^-$ groups create a uniform potential environment for Na^+ cations, leading to a degenerate set of Na^+ site energies (Figs. 5(a) and 5(c)). During $[BH_4]^-$ reorientation, Na–H distances fluctuate markedly, giving rise to distinct local potentials for different Na^+ ions. This fluctuation produces a broadened distribution of Na^+ potential energies — a signature of dynamic frustration (Figs. 5(b) and 5(d)).

The broadening of the Na^+ potential-energy distribution has a dual effect on Na^+ migration. First, certain $[BH_4]^-$ orientations transiently raise the energy of the Na^+ equilibrium site via enhanced Coulombic repulsion, promoting Na^+ delocalization. Second, favorable $[BH_4]^-$ group orientations transiently lower the energy at the saddle point, reducing the effective barrier along specific migration paths. Together, these fluctuations generate numerous transient, spatially and temporally dispersed low-barrier diffusion channels that promote Na^+ delocalization and thereby enhance its migratory capability (Figs. 5(e) and 5(f)).

The Na^+ potential-energy distribution can be quantitatively measured by the density of atomic states (DOAS) by sampling Na^+ atomic energies across MLMD-generated configurations.[44] Initial-state DOAS is constructed from statically relaxed snapshots, where the removal of vibrational displacements isolates the contribution of the local structural en-

vironments around Na^+. Transition-state DOAS is established by performing NEB calculations on the corresponding relaxed configurations to extract the transition-state energies of the same Na^+. This approach captures the modification of the Na^+ potential energy distribution induced by $[BH_4]^-$ reorientation. At 10 K, suppressed reorientation of $[BH_4]^-$ results in an ordered anion lattice and nearly degenerate DOAS, with narrow broadenings of 0.1 eV (initial states) and 0.2 eV (transition states), as shown in Fig. 6(a). It should be noted that these are classical simulation results, as nuclear quantum effects for H^- are not considered. At 400 K, the reorientation of $[BH_4]^-$ generates a quasi-continuum distribution of local Na^+ energies, producing pronounced spectral broadening for both the initial (0.5 eV) and transition (1.0 eV) states, respectively (Fig. 6(b)). The observed increase in DOAS broadening signifies a modulation of Na^+ energy states by $[BH_4]^-$ reorientation. This modulation can elevate the initial-state energy and lower the transition-state energy, collectively forming low-barrier channels that enhance Na^+ migration.

The Na^+ migration barrier distribution, obtained by subtracting the initial-state energies from the transition-state energies in the DOAS, further illustrates this effect. At 10 K, the migration energy barrier distribution is narrow (0.6–0.8 eV) as shown in Fig. 6(c), consistent with the highly degenerate potential energy distributions in the ordered structures (The nuclear quantum effects of H^- are not included in these classical simulations). At 400 K, the broadened Na^+ migration barrier distribution spans from 0.3 eV to 1.8 eV (Fig. 6(d)), with a pronounced lower-energy tail that confirms the reorientation of $[BH_4]^-$ creates low-barrier channels for Na^+ migration.

The formation of low-barrier channels for Na^+ is governed by the translational-rotational mode coupling of the $[BH_4]^-$ anions. When the collective vibrational modes mediated by B^{3+} are suppressed (fixed B^{3+}), both the DOAS and migration-barrier spectra collapse to narrow distributions (Figs. S2 and S3).

The extent of migration-barrier distribution broadening is governed by the interaction strength between anionic groups and cations. In Na_3OBH_4, the reorientation of $[BH_4]^-$ polyanions splits Na^+ migration barriers, but the weak anion-cation interactions constrain the overall broadening, hindering the formation of low-energy migration channels. The absence

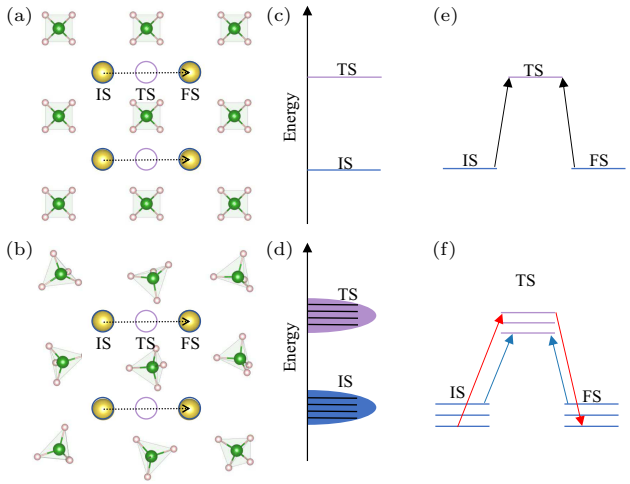

Fig. 5. Mechanism of Na^+ migration enhanced by dynamic frustration. (a) and (b) Schematic illustrations of the Na^+ potential energy landscape within (a) an ordered and (b) a disordered framework of $[BH_4]^-$ groups. (c) and (d) The energy distribution of Na^+ at the initial and transition states, corresponding to the (c) ordered and (d) disordered configurations. (e) and (f) A comparative depiction of the Na^+ migration energy barriers under both conditions, demonstrating the formation of low-energy-barrier pathways induced by the disordered arrangement of $[BH_4]^-$ groups.

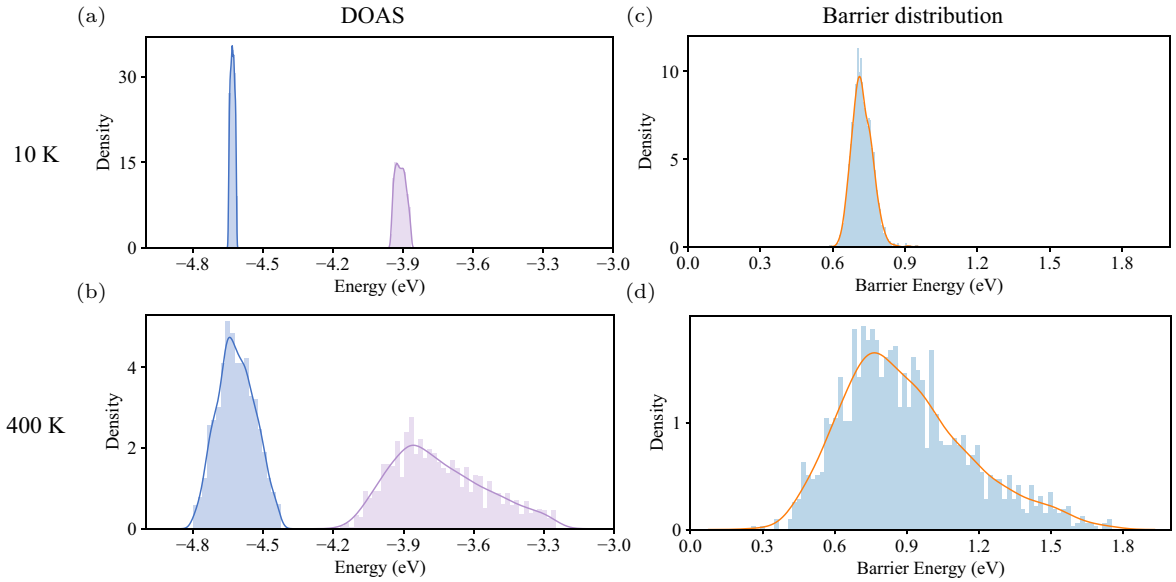

Fig. 6. Comparison of the distributions of the Na^+ energy landscape and migration barriers between ordered and disordered $[BH_4]^-$ groups. (a) and (b) Na^+ potential energy distribution at initial and transition states for (a) 10 K (ordered) and (b) 400 K (disordered). (c) and (d) Corresponding Na^+ migration barrier distributions, illustrating the formation of low-energy-barrier pathways induced by the disordered arrangement of $[BH_4]^-$ groups.

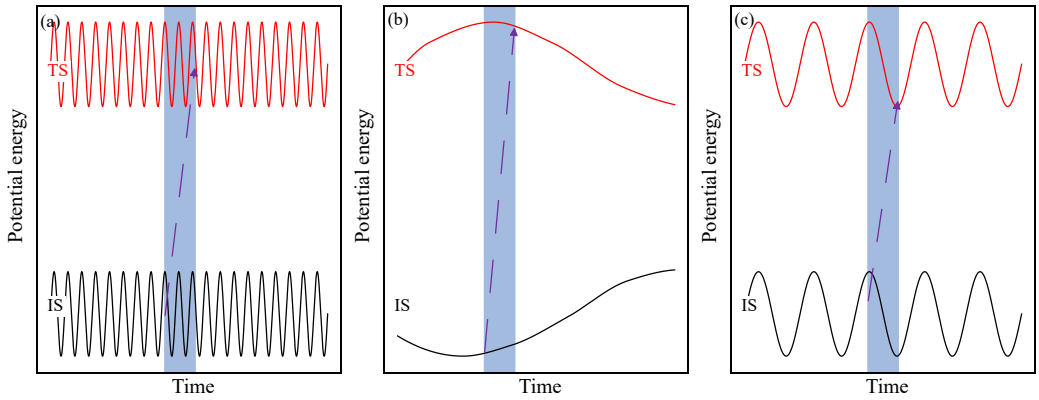

Fig. 7. Frequency correlations between the fluctuations of the carrier potential-energy surface and the carrier vibrational mode. (a) When the fluctuation frequency is much higher than the vibrational frequency, carriers only perceive a time-averaged potential energy; (b) when the fluctuation frequency is much lower than the vibrational frequency, carriers experience a quasi-static potential energy; (c) when the fluctuation frequency is comparable to the vibrational frequency, low-energy-barrier channels are formed, which accelerates ion migration. The black and red curves correspond to the potential-energy fluctuations when the carrier resides in the initial and transition states, respectively. The blue shaded region marks the time scale associated with the transition from the initial state to the transition state.

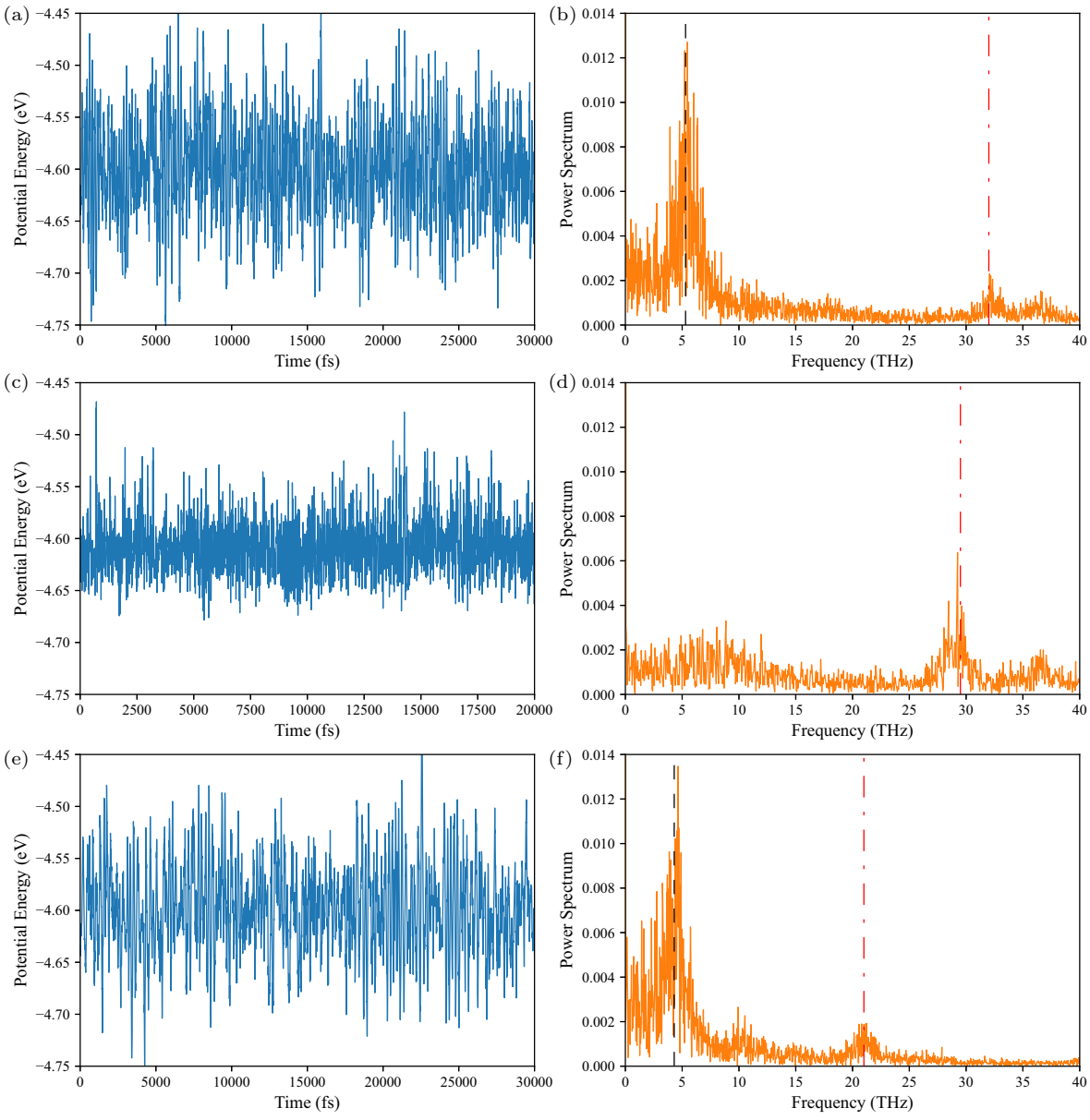

Fig. 8. Dynamic frustration-induced temporal evolution of Na^+ potential energy (left) and corresponding Fourier-transform frequency spectra (right). (a) and (b) Configuration with $^1H^-$ and unconstrained $[BH_4]^-$ collective vibrational modes. (c) and (d) Configuration with $^1H^-$ and constrained $[BH_4]^-$ collective vibrational modes. (e) and (f) Configuration with $^3H^-$ and unconstrained $[BH_4]^-$ collective vibrational modes.

of low-energy migration channels contributes to the low ionic conductivity observed in Na_3OBH_4. Strengthening anion-cation interactions — such as by partially substituting $[BH_4]^-$ with larger (e.g., $[BF_4]^-$) or more polarizable polyanions (e.g., $[NH_2]^-$) — can broaden the distribution of Na^+ migration barriers and promote the formation of low-energy channels that enhance Na^+ transport.

3.5. Frequency correlations under dynamic frustration

The translational-rotational mode of polyanions dynamically perturbs the carrier potential-energy surface. To enhance ionic conductivity, the perturbation frequency of the potential-energy surface must match the Na^+ vibrational frequency. Otherwise, the fluctuations are either averaged out at high frequencies (carriers only perceive a time-averaged potential energy from the anion group reorientation) (Fig. 7(a)) or effectively static at low frequencies (presenting a quasi-static environment) (Fig. 7(b)), providing no improvement in Na^+ transport. Optimal enhancement occurs when the frequencies are comparable: the increase in potential energy induced by dynamical frustration near the equilibrium position promotes Na^+ toward the saddle point, while the subsequent reduction in potential energy near the transition state effectively lowers the barrier and accelerates migration (Fig. 7(c)).

We selected a representative Na^+ ion (Na_{25}) and tracked its potential-energy evolution over time, extracting the perturbation frequencies via Fourier analysis. To isolate the contributions from $[BH_4]^-$ dynamics, Na^+ and O atoms are frozen, with additional freezing of B atoms to separate rotational from total dynamic effects. In the unconstrained $[BH_4]^-$ case, Na^+ experiences potential-energy fluctuations of ~ 0.3 eV, with spectral peaks at 5.5 THz (translational) and 33 THz (rotational) (Figs. 8(a) and 8(b)). Constraining the translational mode reduces the amplitude to 0.15 eV, leaving only the 33 THz rotational peak, indicating that rotations persist while translations contribute the majority of the modulation (Figs. 8(c) and 8(d)). The reduced amplitude indicates that the modulation of Na^+ energy landscape originates from the translational-rotational mode coupling of $[BH_4]^-$ anions. Notably, the rotational perturbation frequency (33 THz) far exceeds the Na^+ vibrational frequency (~ 4 THz), preventing Na^+ from effectively sensing the fast $[BH_4]^-$ motion (Fig. S4). This frequency mismatch likely contributes to the low ionic conductivity observed in Na_3OBH_4.

We performed isotope substitution by replacing H^- with $^3H^-$. The increased atomic mass lowers the $[BH_4]^-$ vibrational frequency from 33 THz to 21 THz, while leaving the perturbation amplitude essentially unchanged (Figs. 8(e) and 8(f)). This shift brings the perturbation frequency closer to the Na^+ vibrational mode, strengthening the dynamic coupling. As a result, the Na^+ migration barrier decreases to 0.24 eV and the diffusivity at 400 K increases by a factor of three (Fig. 9). These results demonstrate that dynamically tuning the potential-energy perturbation frequency can effectively enhance carrier transport in superionic conductors. Through targeted polyanion modification, this frequency-matching coupling under dynamic frustration conditions provides a rational strategy for designing high-performance SSIC materials with optimized transport efficiency.

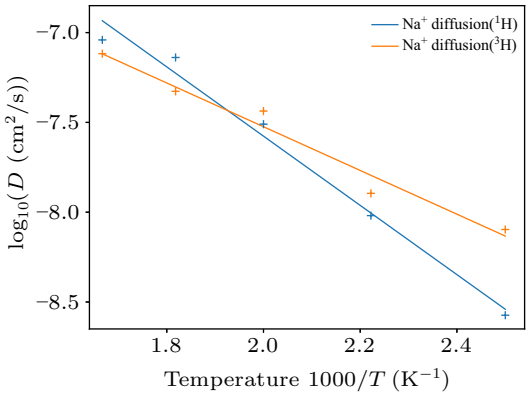

Fig. 9. Arrhenius plots of Na^+ diffusion coefficients comparing systems with $^1H^-$ and $^3H^-$.

4. Conclusion

In this work, MLMD simulations were employed to investigate Na^+ migration in Na_3OBH_4 and to elucidate its coupling with the reorientation dynamics of $[BH_4]^-$ polyanions. The results show that the small reorientation barrier of $[BH_4]^-$ and the weak spatiotemporal correlation between polyanion reorientation and cation migration rule out a paddle-wheel mechanism. Instead, Na^+ migration is governed by dynamic frustration: time-dependent anion reorientation splits the Na^+ energy states and transiently generates low-barrier migration channels. This mechanism is supported by the broadened Na^+ potential-energy distribution in DOAS and by the widened migration-barrier spectrum that reflects barrier-lowering events induced by frustration.

In addition, a Goldilocks-type matching condition is identified between the frequency of Na^+ potential-energy perturbation and the intrinsic Na^+ vibrational frequency. Tuning the $[BH_4]^-$ reorientation timescale via hydrogen isotope substitution strengthens this dynamical coupling, reduces the effective migration barrier, and markedly enhances low-temperature ionic mobility.

These findings reveal two general design principles for superionic conductors based on dynamic frustration: (i) engineering polyanion dynamics to amplify time-dependent PES perturbations, and (ii) matching polyanion-motion frequencies with carrier vibrational modes to maximize resonance-like transport enhancement. These strategies provide a physically grounded pathway toward designing next-generation fast ionic conductors.

Acknowledgments

Project supported by the Natural Science Basic Research Program of Shaanxi Province (Grant No. 2025JC-YBQN-079), the Scientific Research Program of Education Department of Shaanxi Provincial Government (Grant No. 25JK0734), the Startup Foundation for Doctors of Yan'an University (Grant Nos. YDBK2023-58 and YDBK2023-59), and the Yan'an University Innovation and Entrepreneurship Training Program for Undergraduates (Grant No. S202410719137).

References

[1] Zhao C, Liu L, Qi X, Lu Y, Wu F, Zhao J, Yu Y, Hu Y S and Chen L 2018 *Adv. Energy Mater.* **8** 1703012
[2] Janek J and Zeier W G 2016 *Nat. Energy* **1** 16141
[3] Armand M and Tarascon J M 2008 *Nature* **451** 652
[4] Yabuuchi N, Kubota K, Dahbi M and Komaba S 2014 *Chem. Rev.* **114** 11636
[5] Lu Y, Li L, Zhang Q, Niu Z and Chen J 2018 *Joule* **2** 1747
[6] Song S, Duong H M, Korsunsky A M, Hu N and Lu L 2016 *Sci. Rep.* **6** 32330
[7] Duchardt M, Ruschewitz U, Adams S, Dehnen S and Roling B 2018 *Angew. Chem. Int. Ed.* **57** 1351
[8] Zhang Z, Ramos E, Lalère F, Assoud A, Kaup K, Hartman P and Nazar L F 2018 *Energy Environ. Sci.* **11** 87
[9] Hayashi A, Noi K, Tanibata N, Nagao M and Tatsumisago M 2014 *J. Power Sources* **258** 420
[10] Gao J, Zhao Y S, Shi S Q and Li H 2016 *Chin. Phys. B* **25** 018211
[11] Cao Y, Li Y Q and Guo X X 2013 *Chin. Phys. B* **22** 078201
[12] Ji X and Zhang J Q 2023 *Chin. Phys. B* **32** 066601
[13] Lin A M, Shi J, Wei S H and Sun Y Y 2024 *Chin. Phys. B* **33** 086601
[14] Aronsson R, Jansson B, Knape H, Lundén A, Nilsson L, Sjöblom C A and Torell L 1980 *J. Phys. Colloques* **41** 35
[15] Lunden A 1988 *Solid State Commun.* **65** 1237
[16] Wilmer D, Funke K, Witschas M, Banhatti R D, Jansen M, Korus G, Fitter J and Lechner R E 1999 *Phys. B: Condens. Matter* **266** 60
[17] Zhang Z and Nazar L F 2022 *Nat. Rev. Mater.* **7** 389
[18] Sun Y, Wang Y, Liang X, Xia Y, Peng L, Jia H, Li H, Bai L, Feng J, Jiang H and Xie J 2019 *J. Am. Chem. Soc.* **141** 5640
[19] Udovic T J, Matsuo M, Tang W S, Wu H, Stavila V, Soloninin A V, Skoryunov R V, Babanova O A, Skripov A V, Rush J J, Unemoto A, Takamura H and Orimo S 2014 *Adv. Mater.* **26** 7622
[20] Lu Z and Ciucci F 2016 *J. Mater. Chem. A* **4** 17740
[21] Varley J B, Kweon K, Mehta P, Shea P, Heo T W, Udovic T J, Stavila V and Wood B C 2017 *ACS Energy Lett.* **2** 250
[22] Zhang Z, Roy P N, Li H, Avdeev M and Nazar L F 2019 *J. Am. Chem. Soc.* **141** 19360
[23] Smith J G and Siegel D J 2020 *Nat. Commun.* **11** 1483
[24] Wu E A, Banerjee S, Tang H, Richardson P M, Doux J M, Qi J, Zhu Z, Grenier A, Li Y, Zhao E, Deysher G, Sebti E, Nguyen H, Stephens R, Verbist G, Chapman K W, Clément R J, Banerjee A, Meng Y S and Ong S P 2021 *Nat. Commun.* **12** 1256
[25] Wu S, Xiao R, Li H and Chen L 2022 *J. Mater. Chem. A* **10** 3093
[26] Jansen M 1991 *Angew. Chem., Int. Ed. Engl.* **30** 1547
[27] Ahiavi E, Dawson J A, Kudu Ö U, Courty M, Islam M S, Clemens O, Masquelier C and Famprikis T 2020 *J. Power Sources* **471** 228489
[28] He X, Zhu Y, Epstein A and Mo Y 2018 *npj Comput. Mater.* **4** 18
[29] Car R and Parrinello M 1985 *Phys. Rev. Lett.* **55** 2471
[30] Eckhoff M and Behler J 2021 *npj Comput. Mater.* **7** 170
[31] Behler J 2016 *J. Chem. Phys.* **145** 170901
[32] Chan H, Narayanan B, Cherukara M J, Sen F G, Sasikumar K, Gray S K, Chan M K and Sankaranarayanan S K 2019 *J. Phys. Chem. C* **123** 6941
[33] Noé F, Tkatchenko A, Müller K R and Clementi C 2020 *Annu. Rev. Phys. Chem.* **71** 361
[34] Zhang L, Han J, Wang H, Car R and E W 2018 *Phys. Rev. Lett.* **120** 143001
[35] Unke O T, Chmiela S, Sauceda H E, Gastegger M, Poltavsky I, Schütt K T, Tkatchenko A and Müller K R 2021 *Chem. Rev.* **121** 10142
[36] Kohn W and Sham L J 1965 *Phys. Rev.* **140** A1133
[37] Blöchl P E 1994 *Phys. Rev. B* **50** 17953
[38] Perdew J P, Burke K and Ernzerhof M 1998 *Phys. Rev. Lett.* **80** 891
[39] Hoover W G 1985 *Phys. Rev. A* **31** 1695
[40] Zhang Y, Wang H, Chen W, Zeng J, Zhang L, Wang H and E W 2020 *Comput. Phys. Commun.* **253** 107206
[41] Plimpton S 1995 *J. Comput. Phys.* **117** 1
[42] Liu Y, Wu J M, Avdeev M and Shi S Q 2020 *Adv. Theory Simul.* **3** 1900215
[43] Liu Y, Zhao T, Ju W and Shi S 2017 *J. Materiomics* **3** 159
[44] Liu Y, Guo B, Zou X, Li Y and Shi S 2020 *Energy Storage Mater.* **31** 434
[45] Zhao Q, Guo J, Su M, Suo B, Zhu H, Zhou B, Zhang Z and Song Q 2022 *J. Phys. Chem. C* **126** 16546
[46] Tran Qui D, Capponi J J, Gondrand M, Saïb M, Joubert J C and Shannon R D 1981 *Solid State Ionics* **3** 219
[47] Knauth P 2009 *Solid State Ionics* **180** 911
[48] Dawson J A, Canepa P, Famprikis T, Masquelier C and Islam M S 2018 *J. Am. Chem. Soc.* **140** 362
[49] Chandler D 1978 *J. Chem. Phys.* **68** 2959
[50] Xu R and Wunsch D 2005 *IEEE Trans. Neural Netw.* **16** 645
[51] Di Stefano D, Miglio A, Robeyns K, Filinchuk Y, Lechartier M, Senyshyn A, Ishida H, Spannenberger S, Prutsch D, Lunghammer S, Rettenwander D, Wilkening M, Roling B, Kato Y and Hautier G 2019 *Chem* **5** 2450
[52] Kweon K E, Varley J B, Shea P, Adelstein N, Mehta P, Heo T W, Udovic T J, Stavila V and Wood B C 2017 *Chem. Mater.* **29** 9142
[53] Wang S, Liu Y and Mo Y 2023 *Angew. Chem. Int. Ed.* **62** e202215544